2

Computational Strategies for Standard Soil Plasticity Models

René de Borst and **Arend E. Groen**
Delft University of Technology, The Netherlands

2.1 Introduction

Since the early developments in the 1950s and 1960s by Drucker and Prager and by the Cambridge school, plasticity theory has become an established framework for modeling the inelastic behavior of soils. Nowadays, it has earned a broad interest and acceptance (Drucker *et al.*, 1957; Roscoe and Burland, 1968; Matsuoka and Nakai, 1974; Lade, 1977; Desai, 1980). The Cam-Clay model (Roscoe and Schofield, 1963) has become widely accepted as a constitutive model that pairs a relative simplicity – and therefore a limited number of parameters – to a description of the essential mechanical properties of clays. For sand under monotonic loading, double-hardening models (Lade, 1977) have become popular. In these models, a shear yield surface is complemented by a cap, which limits the hydrostatic stresses and enables capturing the inelastic straining under pure compaction. Typically, these sand models are furnished with a non-associative flow rule, a hardening curve with a hyperbolic shape, and elastic moduli that are stress-level dependent.

Both classes of constitutive models – Cam-Clay models and double-hardening models – have a yield surface that is dependent on the hydrostatic stress level and are equipped with stress-level dependent elastic moduli. Furthermore, the Cam-Clay model possesses a non-associative hardening rule, while double-hardening models typically are furnished with a non-associative flow rule. In either case, this leads to a non-symmetric tangential matrix for the incremental relation between stress rate and strain rate. Because of this lack of symmetry, and because of the highly nonlinear nature of both classes of constitutive models, an explicit integration will only be conditionally stable. Nonetheless, most integration procedures utilize an explicit procedure (Britto and Gunn, 1989; Desai *et al.*, 1991; Hicks, 1995). Since the early 1990s, a few attempts have been made to apply implicit integration to plasticity models for soils (Borja, 1991; Hofstetter *et al.*, 1993; Simo *et al.*, 1993). Such an integration procedure allows for much larger loading

steps. Moreover, the resulting algorithm is, in general, amenable to exact linearization, which ensures quadratic convergence when a Newton–Raphson strategy is applied on structural level.

This contribution is ordered as follows. After a brief introduction into plasticity theory, we shall formulate a fully implicit Euler backward return-mapping algorithm originally proposed by Borja (1991) which incorporates the use of stress invariants as primary variables and a secant update for the elastic properties. The algorithm will be applied for the integration of the Modified Cam-Clay model and a double-hardening model for sand. The numerical performance and robustness will be demonstrated by simulation of common laboratory tests and realistic boundary value problems, i.e. the simulation of a guided pipe-jacking in soft clay and an analysis of the Leaning Tower of Pisa.

## 2.2   A Note on Stress and Strain Definitions

In almost all soil mechanics applications, only compressive stresses are present. Therefore, it would be convenient to use a sign convention in which compressive stresses are positive (Figure 2.1(a)). On the other hand, in a general purpose finite element code, tensile stresses are usually regarded positive (Figure 2.1(b)). As the objective is to demonstrate how elasto-plastic soil models can be conveniently implemented into a general-purpose finite element code, it is assumed that tensile stresses are positive.

The stress tensor $\boldsymbol{\sigma}$ and the strain tensor $\boldsymbol{\varepsilon}$ are introduced in a vector format as

$$\boldsymbol{\sigma} = [\sigma_{xx}, \sigma_{yy}, \sigma_{zz}, \sigma_{xy}, \sigma_{yz}, \sigma_{zx}]^{\mathrm{T}} \tag{2.1}$$

$$\boldsymbol{\varepsilon} = [\varepsilon_{xx}, \varepsilon_{yy}, \varepsilon_{zz}, 2\varepsilon_{xy}, 2\varepsilon_{yz}, 2\varepsilon_{zx}]^{\mathrm{T}} \tag{2.2}$$

in which the engineering shear strains have been utilized instead of the tensorial shear strains. The hydrostatic pressure and the volumetric strain are defined as

(a)   (b)
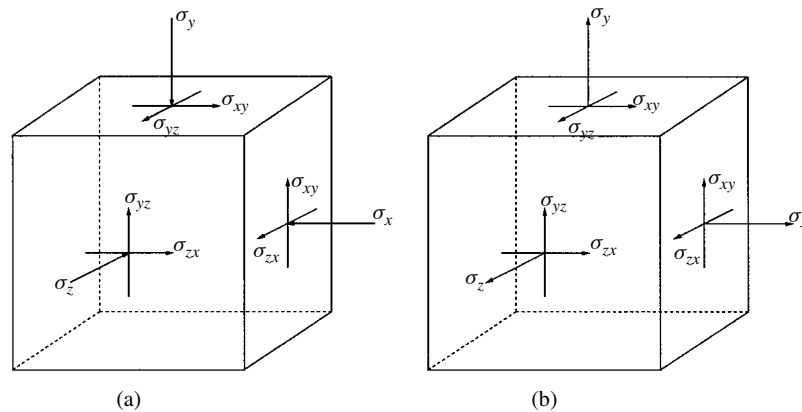
Figure 2.1   Possible sign conventions for the stress tensor. (a) Sign convention normally utilized in soil mechanics. Compression is regarded positive. (b) Sign convention normally utilized in finite element codes and utilized in this contribution. Tension is regarded positive

$$p = \tfrac{1}{3}(\sigma_{xx} + \sigma_{yy} + \sigma_{zz}) \tag{2.3}$$

$$\varepsilon_v = \varepsilon_{xx} + \varepsilon_{yy} + \varepsilon_{zz} \tag{2.4}$$

in which p is the hydrostatic tensile component and ε_v is the volumetric strain. Upon introduction of the projection vector $\boldsymbol{\pi} = [1, 1, 1, 0, 0, 0]^{\mathrm{T}}$, one can define the deviatoric stresses ($\boldsymbol{\xi}$) and strains ($\boldsymbol{\gamma}$),

$$\boldsymbol{\xi} = \boldsymbol{\sigma} - p\boldsymbol{\pi} \tag{2.5}$$

$$\boldsymbol{\gamma} = \boldsymbol{\varepsilon} - \tfrac{1}{3}\varepsilon_v\boldsymbol{\pi} \tag{2.6}$$

The effective deviatoric stress (q) is defined according to

$$q = \sqrt{\tfrac{3}{2}\boldsymbol{\xi}^{\mathrm{T}}\boldsymbol{R}\boldsymbol{\xi}}; \quad \boldsymbol{R} = \mathrm{diag}[1, 1, 1, 2, 2, 2] \tag{2.7}$$

The Lode angle θ is defined as

$$\cos 3\theta = -\frac{27}{2}\frac{J_3}{q^3}; \quad J_3 = \xi_{xx}\xi_{yy}\xi_{zz} + \xi_{xy}\xi_{yz}\xi_{zx} - 2(\xi_{xx}\xi_{yz}^2 + \xi_{yy}\xi_{zx}^2 + \xi_{zz}\xi_{xy}^2) \tag{2.8}$$

2.3 Computational Plasticity

A fundamental notion in plasticity theory is the existence of a yield function that bounds the elastic domain. Plasticity can only occur if the stresses $\boldsymbol{\sigma}$ satisfy the general yield criterion

$$f(\boldsymbol{\sigma}, \kappa) = 0 \tag{2.9}$$

where the hardening variable κ controls the amount of hardening or softening. Plastic behavior is characterized by the presence of irreversible strains upon load removal. These are introduced via the usual decomposition of the strain rate vector $\dot{\boldsymbol{\varepsilon}}$ in an elastic, reversible contribution $\dot{\boldsymbol{\varepsilon}}^{\mathrm{e}}$ and a plastic, irreversible contribution $\dot{\boldsymbol{\varepsilon}}^{\mathrm{p}}$:

$$\dot{\boldsymbol{\varepsilon}} = \dot{\boldsymbol{\varepsilon}}^{\mathrm{e}} + \dot{\boldsymbol{\varepsilon}}^{\mathrm{p}} \tag{2.10}$$

The elastic strain rate is related to the stress rate by an elastic constitutive law

$$\dot{\boldsymbol{\sigma}} = \boldsymbol{E}^{\mathrm{t}}(\boldsymbol{\varepsilon}^{\mathrm{e}})\dot{\boldsymbol{\varepsilon}}^{\mathrm{e}} \tag{2.11}$$

It is assumed that the tangential elastic stiffness matrix $\boldsymbol{E}^{\mathrm{t}}(\boldsymbol{\varepsilon}^{\mathrm{e}})$ is solely dependent on the elastic strain field $\boldsymbol{\varepsilon}^{\mathrm{e}}$. The assumption of a non-associative flow rule yields

$$\dot{\boldsymbol{\varepsilon}}^{\mathrm{p}} = \dot{\lambda}\frac{\partial g(\boldsymbol{\sigma}, \kappa)}{\partial \boldsymbol{\sigma}} \tag{2.12}$$

where $g(\boldsymbol{\sigma}, \kappa)$ is the plastic potential function and $\dot{\lambda}$ is the (rate of the) plastic multiplier. The hardening variable κ is defined in a rate form as

$$\dot{\kappa} = \dot{\kappa}(\boldsymbol{\sigma}, \dot{\boldsymbol{\varepsilon}}^{\mathrm{p}}) \tag{2.13}$$

on the basis of which a number of different measures for $\dot{\kappa}$ can be postulated. This contribution is restricted to strain hardening

$$\dot{\kappa} = \dot{\kappa}(\dot{\boldsymbol{\varepsilon}}^{\mathrm{p}}) \tag{2.14}$$

which is integrated along the loading path to give

$$\kappa = \int_0^t \dot{\kappa} \, d\tau \tag{2.15}$$

Loading/unloading is conveniently established in Kuhn–Tucker form

$$\dot{\lambda} \geq 0; \quad f \leq 0; \quad \dot{\lambda} f = 0 \tag{2.16}$$

Neither the yield function in Eq. (2.9) nor the plastic potential $g(\boldsymbol{\sigma}, \kappa)$ in Eq. (2.12) need to be C_1 continuous. In fact, the assumption of only piecewise C_1 continuous yield functions and plastic potentials allows for an independent description of different irreversible phenomena within one material. For example, tensile failure and compressive crushing can be treated independently for concrete (Feenstra, 1993), or for masonry (Lourenço, 1996). In this contribution, piecewise C_1 continuous yield functions and plastic potentials will be adopted for modeling shear failure and irrecoverable compression independently. Before elaborating the details of the constitutive modeling, a possible description of plasticity with only piecewise C_1 continuous yield functions and plastic potentials will be presented.

Assume that the yield function is described by a set of C_1 continuous yield functions

$$f_i(\boldsymbol{\sigma}, \kappa_i) \leq 0 \tag{2.17}$$

in which κ_i is the hardening variable representative for plastic flow on that C_1 continuous yield surface. The additive decomposition of the strain rate given by Eq. (2.10) is generalized to (Koiter, 1953)

$$\dot{\boldsymbol{\varepsilon}} = \dot{\boldsymbol{\varepsilon}}^{\mathrm{e}} + \sum_{i=1}^{i=n} \dot{\varepsilon}_i^{\mathrm{p}} \tag{2.18}$$

with

$$\dot{\boldsymbol{\varepsilon}}_i^{\mathrm{p}} = \dot{\lambda}_i \frac{\partial g_i(\boldsymbol{\sigma}, \kappa_i)}{\partial \boldsymbol{\sigma}} \tag{2.19}$$

$g_i(\boldsymbol{\sigma}, \kappa_i)$ is a C_1 continuous plastic potential, which governs the flow direction on each C_1 continuous yield function f_i. Like in single surface plasticity, κ_i is integrated along the loading path

$$\kappa_i = \int_0^t \dot{\kappa}_i(\dot{\boldsymbol{\varepsilon}}_i^{\mathrm{p}}) \, d\tau \tag{2.20}$$

The Kuhn–Tucker conditions defined by Eq. (2.16) are generalized to

$$\dot{\lambda}_i \geq 0; \quad f_i \leq 0; \quad \dot{\lambda}_i f_i = 0 \tag{2.21}$$

2.3.1   Return-mapping via invariants with use of elastic secant moduli

The integration of the rate equations resulting from flow theory can be regarded as follows. At stage n the stresses, the total and elastic strains and the hardening parameter(s) are known. The objective is to determine the update of these parameters

$$\{\boldsymbol{\sigma}_n, \boldsymbol{\varepsilon}_n, \boldsymbol{\varepsilon}_n^{\mathrm{e}}, \kappa_{i,n}\} \rightarrow \{\boldsymbol{\sigma}_{n+1}, \boldsymbol{\varepsilon}_{n+1}, \boldsymbol{\varepsilon}_{n+1}^{\mathrm{e}}, \kappa_{i,n+1}\} \tag{2.22}$$

in which the subscript $n + 1$ refers to the new, yet unknown state. In the remainder, the subscript $n + 1$ will be dropped where convenient. Within the framework of a finite element code based on the displacement method, the total strains are updated according to

$$\boldsymbol{\varepsilon}_{n+1} = \boldsymbol{\varepsilon}_n + \Delta\boldsymbol{\varepsilon} \tag{2.23}$$

in which the incremental strain $\Delta\boldsymbol{\varepsilon}$ is determined from the strain-displacement relation $\Delta\boldsymbol{\varepsilon} = \boldsymbol{B}\,\Delta\mathbf{a}$, with $\Delta\mathbf{a}$ the nodal displacement increments for the respective element and $\boldsymbol{B}$ the strain-displacement operator in a typical integration (sampling) point for the respective element*. Henceforth, an integration algorithm based on Eq. (2.23) will be referred to as 'strain-driven'. What remains is to determine $\{\boldsymbol{\sigma}_{n+1}, \boldsymbol{\varepsilon}_{n+1}^{\mathrm{e}}, \kappa_{i,n+1}\}$ with the constraint given by the update of $\boldsymbol{\varepsilon}_{n+1}$ in Eq. (2.23).

The additive decomposition of the strain rate in Eq. (2.18) is now generalized to strain increments

$$\Delta\boldsymbol{\varepsilon} = \Delta\boldsymbol{\varepsilon}^{\mathrm{e}} + \sum_{i=1}^{i=n} \Delta\boldsymbol{\varepsilon}_i^{\mathrm{p}} \tag{2.24}$$

The elastic contribution to the strain increment is determined by the elastic constitutive law

$$\boldsymbol{\sigma}_{n+1} = \boldsymbol{\sigma}_n + \overline{\boldsymbol{E}}(\boldsymbol{\varepsilon}_n^{\mathrm{e}}, \boldsymbol{\varepsilon}_{n+1}^{\mathrm{e}})\Delta\boldsymbol{\varepsilon}^{\mathrm{e}} \tag{2.25}$$

in which $\overline{\boldsymbol{E}}$ is the *secant* elastic stiffness matrix. The plastic contribution to the strain increment is determined by the flow rule

$$\Delta\boldsymbol{\varepsilon}_i^{\mathrm{p}} = \Delta\lambda_i \frac{\partial g_i(\boldsymbol{\sigma}_{n+1}, \kappa_{i,n+1})}{\partial\boldsymbol{\sigma}_{n+1}} \tag{2.26}$$

in which the hardening variable $\kappa_{i,n+1}$ at the end of a step is determined by generalization of the integral in Eq. (2.20) for a finite increment

$$\kappa_{i,n+1} = \kappa_{i,n} + \Delta\kappa_i(\Delta\boldsymbol{\varepsilon}_i^{\mathrm{p}}) \tag{2.27}$$

It has been shown by Simo *et al.* (1988) that an Euler backward integration algorithm is equivalent to a constrained optimization problem governed by discrete Kuhn–Tucker conditions:

$$\Delta\lambda_i \geq 0; \quad f_i(\boldsymbol{\sigma}_{n+1}, \kappa_{i,n+1}) \leq 0; \quad \Delta\lambda_i f_i(\boldsymbol{\sigma}_{n+1}, \kappa_{i,n+1}) = 0 \tag{2.28}$$

---

*Applicable to standard isoparametric elements. For $\overline{\boldsymbol{B}}$-elements (Hughes, 1980) the strain-displacement relation takes a slightly different form. The strain increment $\Delta\boldsymbol{\varepsilon}$ is then determined as $\Delta\boldsymbol{\varepsilon} = \overline{\boldsymbol{B}}\,\Delta\mathbf{a}$.

Algorithmically, it is assumed that initially all deformations are elastic,

$$\boldsymbol{\varepsilon}^{e}_{\text{trial}} = \boldsymbol{\varepsilon}^{e}_{n} + \Delta\boldsymbol{\varepsilon}; \quad \Delta\lambda_{i,\text{trial}} = 0 \tag{2.29}$$

which results in the elastic 'trial' stress

$$\boldsymbol{\sigma}_{\text{trial}} = \boldsymbol{\sigma}_{n} + \overline{\boldsymbol{E}}(\boldsymbol{\varepsilon}^{e}_{n}, \boldsymbol{\varepsilon}^{e}_{\text{trial}})\Delta\boldsymbol{\varepsilon} \tag{2.30}$$

and in an estimate for the hardening variable(s)

$$\Delta\kappa_{i,\text{trial}} = 0 \rightarrow \kappa_{i,\text{trial}} = \kappa_{i,n} \tag{2.31}$$

Violation of any of the yield functions $f_i(\boldsymbol{\sigma}_{\text{trial}}, \kappa_{i,\text{trial}}) \leq 0$ determines which flow system is active. Then, Eqs. (2.24)–(2.28) are solved for these active flow systems under condition of Eq. (2.23) with the requirement that the yield function representative for the active flow system is enforced rigorously

$$f_i(\boldsymbol{\sigma}_{n+1}, \kappa_{1,n+1}) = 0 \tag{2.32}$$

and with initial conditions defined by Eqs. (2.29)–(2.31). If none of the yield functions is violated then the trial stress state in Eq. (2.30) lies in the elastic domain and the update in Eq. (2.22) is given by the initial state in Eqs. (2.29)–(2.31) and condition in Eq. (2.23).

Rigorous enforcement of the active yield function(s) given by Eq. (2.32) combined with the initial state defined by Eqs. (2.29)–(2.31) can be interpreted as an elastic 'trial' stress being 'mapped back' onto the yield surface(s) representative for the active flow system(s). Therefore, the name 'Euler backward return-mapping' has been coined. It has been shown in different studies (e.g. Ortiz and Popov, 1985; and Simo and Taylor, 1986) that the implicit Euler backward return-mapping algorithm is unconditionally stable and accurate for J_2-plasticity. However, even when the yield surface is highly distorted, the Euler Backward algorithm is stable (Ortiz and Popov, 1985) and accurate (de Borst and Feenstra, 1990; Schellekens and de Borst, 1990).

For convenience in soil mechanics, the stresses and strains are decomposed into volumetric and deviatoric contributions. The additive decomposition in Eq. (2.24) is separated into a volumetric and a deviatoric part

$$\Delta\varepsilon_v = \Delta\varepsilon_v^e + \sum_{i=1}^{i=n} \Delta\varepsilon_{v,i}^p; \quad \Delta\boldsymbol{\gamma} = \Delta\boldsymbol{\gamma}^e + \sum_{i=1}^{i=n} \Delta\boldsymbol{\gamma}_i^p \tag{2.33}$$

The volumetric and deviatoric plastic strain increments are determined by

$$\Delta\varepsilon_{v,i}^p = \Delta\lambda_i \frac{\partial g_i}{\partial p}; \quad \Delta\boldsymbol{\gamma}_i^p = \Delta\lambda_i \frac{\partial g_i}{\partial \boldsymbol{\xi}} \tag{2.34}$$

in which it is assumed that the plastic potential g_i is solely a function of the first and the second stress invariants and of the hardening variable, i.e.

$$g_i = g_i(p, q, \kappa_i) \tag{2.35}$$

Equation (2.35) covers a wide range of plastic potentials that are applicable to soils, including for example the Modified Cam-Clay model (Roscoe and Burland, 1968). Note

that still $f_i = f_i(p, q, \cos 3\theta, \kappa_i)$. With the assumption of isotropy, the volumetric and deviatoric elastic strain increment are determined by

$$p = p_n + \overline{K} \Delta \varepsilon_v^e; \quad \boldsymbol{\xi} = \boldsymbol{\xi}_n + 2\overline{G} \boldsymbol{R}^{-1} \Delta \boldsymbol{\gamma}^e \tag{2.36}$$

in which $\overline{K}$ and $\overline{G}$ are the *secant* elastic bulk modulus and shear modulus, respectively. For computational convenience, it is assumed that both $\overline{K}$ and $\overline{G}$ are solely dependent on the elastic volumetric strain ε_v^e. This restriction yields the following form for the elastic secant moduli

$$\overline{K} = \overline{K} \left(\varepsilon_{v,n}^e, \varepsilon_{v,n}^e + \Delta \varepsilon_v - \sum_{i=1}^{i=n} \Delta \lambda_i \frac{\partial g_i}{\partial p} \right) \tag{2.37}$$

$$\overline{G} = \overline{G} \left(\varepsilon_{v,n}^e, \varepsilon_{v,n}^e + \Delta \varepsilon_v - \sum_{i=1}^{i=n} \Delta \lambda_i \frac{\partial g_i}{\partial p} \right) \tag{2.38}$$

Combination of Eqs. (2.33), (2.34) and (2.36) allows the evolution of the hydrostatic pressure to be written as

$$p = p_n + \overline{K} \left[\Delta \varepsilon_v - \sum_{i=1}^{i=n} \Delta \lambda_i \frac{\partial g_i}{\partial p} \right] \tag{2.39}$$

Similarly, combination of Eqs. (2.33), (2.34) and (2.36) gives for the deviatoric part

$$\boldsymbol{\xi} = \boldsymbol{\xi}_n + 2\overline{G} \boldsymbol{R}^{-1} \left[\Delta \boldsymbol{\gamma} - \sum_{i=1}^{i=n} \Delta \lambda_i \frac{\partial g_i}{\partial \boldsymbol{\xi}} \right] \tag{2.40}$$

The assumption for the plastic potential in Eq. (2.35) leads to the following convenient form for the plastic flow direction in the deviatoric plane

$$\frac{\partial g_i}{\partial \boldsymbol{\xi}} = m_i \boldsymbol{R} \boldsymbol{\xi} \tag{2.41}$$

in which $m_i = m_i(p, q, \kappa_i)$ is a scalar function. Equations (2.40) and (2.41) now yield an explicit expression for the deviatoric stress update

$$\boldsymbol{\xi} = \left[1 + 2\overline{G} \sum_{i=1}^{i=n} \Delta \lambda_i m_i \right]^{-1} [\boldsymbol{\xi}_n + 2\overline{G} \boldsymbol{R}^{-1} \Delta \boldsymbol{\gamma}] \tag{2.42}$$

The actual integration algorithm as proposed by Borja (1991) can now be written in the following way:

$$\boldsymbol{r} = \boldsymbol{r}(\boldsymbol{a}(\boldsymbol{\varepsilon}), \boldsymbol{\xi}(\boldsymbol{a}, \boldsymbol{\varepsilon}), \boldsymbol{\varepsilon})) \tag{2.43}$$

with $\boldsymbol{a} = [p, q, \cos 3\theta, \overline{G}, \Delta \kappa_i, \Delta \lambda_i]^T$. The set of residuals $\boldsymbol{r}$ is defined by

$$\boldsymbol{r}^T = [\boldsymbol{r}_1, \boldsymbol{r}_2, \boldsymbol{r}_3, \boldsymbol{r}_4]^T \tag{2.44}$$

In r_1, the update of the stress invariants is collected

$$r_1 = \begin{bmatrix} p - p\left(\Delta\varepsilon_v - \sum_{i=1}^{i=n} \Delta\lambda_i \frac{\partial g_i}{\partial p}\right) \\ q - \sqrt{\frac{3}{2}\boldsymbol{\xi}^{\mathrm{T}}\boldsymbol{R}\boldsymbol{\xi}} \\ \cos 3\theta + \frac{27}{2} \frac{\xi_{xx}\xi_{yy}\xi_{zz} + \xi_{xy}\xi_{yz}\xi_{zx} - 2(\xi_{xx}\xi_{yz}^2 + \xi_{yy}\xi_{zx}^2 + \xi_{zz}\xi_{xy}^2)}{q^3} \end{bmatrix} \tag{2.45}$$

in which $\boldsymbol{\xi}$ is determined from the explicit update presented in Eq. (2.42). r_2 contains the evolution of the secant shear modulus

$$r_2 = \overline{G} - \overline{G}\left(\Delta\varepsilon_v - \sum_{i=1}^{i=n} \Delta\lambda_i \frac{\partial g_i}{\partial p}\right) \tag{2.46}$$

r_3 contains the evolution of the increment of the hardening variables

$$\boldsymbol{r}_3 = \Delta\kappa_i - \Delta\kappa_i\left(\Delta\lambda_i \frac{\partial g_i}{\partial p}, \Delta\lambda_i m_i \boldsymbol{R}\boldsymbol{\xi}\right) \tag{2.47}$$

and $\boldsymbol{r}_4$ represents the active/inactive flow systems

$$\boldsymbol{r}_4 = f_i(p, q, \cos 3\theta, \Delta\kappa_i) \text{ or } \boldsymbol{r}_4 = \Delta\lambda_i \tag{2.48}$$

in which $\boldsymbol{r}_4 = f_i$ when the representative flow system is active and $\boldsymbol{r}_4 = \Delta\lambda_i$ when the representative flow system is inactive. The determination of which flow system is active will be addressed at the end of this section.

Under the condition that $\boldsymbol{\varepsilon}$ is constant, the set in Eq. (2.43) can be solved with a Newton–Raphson iterative scheme

$$\delta\boldsymbol{a} = -\left[\frac{\partial\boldsymbol{r}}{\partial\boldsymbol{a}} + \frac{\partial\boldsymbol{r}}{\partial\boldsymbol{\xi}}\frac{\partial\boldsymbol{\xi}}{\partial\boldsymbol{a}}\right]^{-1}\delta\boldsymbol{r} \tag{2.49}$$

To complete the return-mapping algorithm, it is assumed that the initial conditions for the solution of system of Eqs. (2.45)–(2.48) and the deviatoric stress update in Eq. (2.42) are defined by the elastic 'trial' state, c.f. Eqs. (2.29)–(2.31). In terms of the governing quantities this yields

$$\begin{bmatrix} p_{\mathrm{trial}} \\ q_{\mathrm{trial}} \\ (\cos 3\theta)_{\mathrm{trial}} \end{bmatrix} = \begin{bmatrix} p(\Delta\varepsilon_v) \\ \sqrt{\frac{3}{2}\boldsymbol{\xi}_{\mathrm{trial}}^{\mathrm{T}}\boldsymbol{R}\boldsymbol{\xi}_{\mathrm{trial}}} \\ -\frac{27}{2} \frac{\{\xi_{xx}\xi_{yy}\xi_{zz} + \xi_{xy}\xi_{yz}\xi_{zx} - 2(\xi_{xx}\xi_{yz}^2 + \xi_{yy}\xi_{zx}^2 + \xi_{zz}\xi_{xy}^2)\}_{\mathrm{trial}}}{q_{\mathrm{trial}}^3} \end{bmatrix} \tag{2.50}$$

in which $\boldsymbol{\xi}_{\mathrm{trial}}$ is determined by

$$\boldsymbol{\xi}_{\mathrm{trial}} = [\boldsymbol{\xi}_n + 2\overline{G}_{\mathrm{trial}}\boldsymbol{R}^{-1}\Delta\boldsymbol{\gamma}]; \quad \overline{G}_{\mathrm{trial}} = \overline{G}(\Delta\varepsilon_v) \tag{2.51}$$

Furthermore,

$$\Delta\kappa_{i,\mathrm{trial}} = 0; \quad \Delta\lambda_{i,\mathrm{trial}} = 0 \tag{2.52}$$

A problem that remains is how to determine which flow system (cf. Eq. (2.48)) is active. In this chapter, a trial and error procedure has been adopted. It is assumed that the initial active flow systems are defined by the trial state ($f_{i,\text{trial}} \geq 0$). If, after completion, any $\Delta\lambda_i \geq 0$ or $f_i \leq 0$ is found, the number of active flow systems is adjusted accordingly and the return-mapping algorithm is restarted.

Remarks
- The algorithm presented can easily be adapted for explicit coupling effects (Feenstra, 1993; Lourenço, 1996). The set of residuals r_3 in Eq. (2.47) is then modified to

$$r_3 = \Delta\kappa_i - C_{ij}\Delta\kappa_j \left(\Delta\lambda_i \frac{\partial g_i}{\partial p}, \Delta\lambda_i m_i R \xi \right) \tag{2.53}$$

  in which C_{ij} is a set of coupling terms, for example discussed in Lourenço (1996) regarding tensile and shear failure in masonry joints.

- The shear and bulk moduli indicated in Eqs. (2.37) and (2.38) may lead to a non-conservative elastic contribution, in which energy may be extracted from certain loading cycles (Zytinsky *et al.*, 1978). However, this fact may not be too important when monotonic loading is considered (Borja, 1991).

2.3.2   Tangential linearization

On basis of the integration algorithm, a consistent tangential operator is formulated. For this purpose, the stress update following from the solution of system of Eqs. (2.45)–(2.48) and the deviatoric stress update in Eq. (2.42) is written as

$$\sigma = \sigma_n + \xi(a(\varepsilon), \varepsilon) + \pi p(a(\varepsilon)) \tag{2.54}$$

which can be differentiated straightforwardly as

$$\frac{d\sigma}{d\varepsilon} = \frac{\partial \xi}{\partial \varepsilon} + \frac{\partial \xi}{\partial a}\frac{da}{d\varepsilon} + \pi\frac{\partial p}{\partial a}\frac{da}{d\varepsilon} = \frac{\partial \xi}{\partial \varepsilon} + \left[\frac{\partial \xi}{\partial a} + \pi\frac{\partial p}{\partial a}\right]\frac{da}{d\varepsilon} \tag{2.55}$$

Equation (2.55) contains only partial derivatives except for $da/d\varepsilon$. The latter quantities can be determined implicitly from the fact that the strain is constant during integration. Thus,

$$\frac{dr}{d\varepsilon} = \left[\frac{\partial r}{\partial a} + \frac{\partial r}{\partial \xi}\frac{\partial \xi}{\partial a}\right]\frac{da}{d\varepsilon} + \frac{\partial r}{\partial \xi}\frac{\partial \xi}{\partial \varepsilon} + \frac{\partial r}{\partial \varepsilon} = 0 \rightarrow$$

$$\frac{da}{d\varepsilon} = -\left[\frac{\partial r}{\partial a} + \frac{\partial r}{\partial \xi}\frac{\partial \xi}{\partial a}\right]^{-1}\left[\frac{\partial r}{\partial \xi}\frac{\partial \xi}{\partial \varepsilon} + \frac{\partial r}{\partial \varepsilon}\right] \tag{2.56}$$

in which the inverse term between brackets is available from the return-mapping algorithm, Eq. (2.49). Substitution of $da/d\varepsilon$ according to Eq. (2.56) into Eq. (2.55) gives the desired form for the consistent tangential operator

$$\frac{d\sigma}{d\varepsilon} = \frac{\partial \xi}{\partial \varepsilon} - \left[\frac{\partial \xi}{\partial a} + \pi\frac{\partial p}{\partial a}\right]\left[\frac{\partial r}{\partial a} + \frac{\partial r}{\partial \xi}\frac{\partial \xi}{\partial a}\right]^{-1}\left[\frac{\partial r}{\partial \xi}\frac{\partial \xi}{\partial \varepsilon} + \frac{\partial r}{\partial \varepsilon}\right] \tag{2.57}$$

2.4   Modeling of Clay

Cam-Clay models originate from the work of Roscoe and his co-workers at the University of Cambridge (Roscoe and Schofield, 1963; Schofield and Wroth, 1968). The original idea was further developed by Roscoe and Burland (1968) to the Modified Cam-Clay model; nowadays, the most widely used elasto-plastic model for the description of the mechanical behavior of clay.

The advantage of the Modified Cam-Clay model lies in its apparent simplicity and its capability to represent (at least qualitatively) the strength and deformation properties of clay realistically. Commonly observed properties such as an increasing stiffness as the material undergoes compression, hardening/softening and compaction/dilatancy behavior, and the tendency to eventually reach a state in which the strength and volume become constant are all captured by the Modified Cam-Clay model. Moreover, calibration of the model requires only a few conventional laboratory tests.

The material description starts most conveniently with the hydrostatic components. The increasing bulk stiffness for increasing compression is modeled by

$$\dot{p} = -\frac{p}{\lambda^*}\dot{\varepsilon}_v = K_t\dot{\varepsilon}_v \text{ loading} \tag{2.58}$$

$$\dot{p} = -\frac{p}{\kappa^*}\dot{\varepsilon}_v = K_t\dot{\varepsilon}_v \text{ unloading} \tag{2.59}$$

λ^* and κ^* will be referred to as the 'modified compression index' and the 'modified swelling index', respectively (Figure 2.2(a)). As unloading is assumed to be elastic Eq. (2.59) can be expressed using elastic components only

$$\dot{p} = -\frac{p}{\kappa^*}\dot{\varepsilon}_v^e = K_t\dot{\varepsilon}_v^e \tag{2.60}$$

For three-dimensional stress states also deviatoric components have to be specified. When Eq. (2.60) is taken as a point of departure the assumption of isotropy, together with a constant Poisson's ratio v, gives

$$G_t = \frac{3}{2}\frac{1-2v}{1+v}K_t \tag{2.61}$$
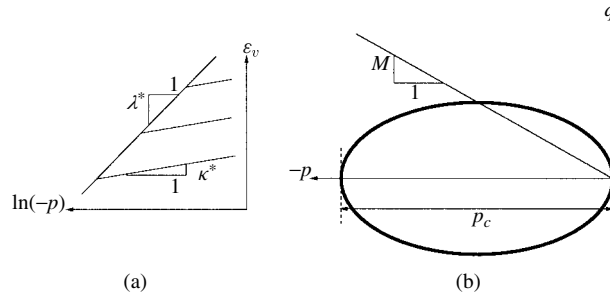
Figure 2.2   Material description for Modified Cam-Clay. (a) Compressive behavior. (b) Yield function and plastic potential

The yield function (f) is given by the expression

$$f = q^2 + M^2 p(p + p_c) \tag{2.62}$$

in which p_c is the preconsolidation pressure (Figure 2.2(b)). Associative plasticity is assumed so that Eq. (2.62) also defines the plastic potential. Consequently, the plastic volumetric strain rate $\dot{\varepsilon}_v^{\mathrm{p}}$ is given by

$$\dot{\varepsilon}_v^{\mathrm{p}} = \dot{\lambda}\frac{\partial f}{\partial p} = \dot{\lambda}M^2(2p + p_c) \tag{2.63}$$

The deviatoric plastic strain rate $\dot{\boldsymbol{\gamma}}^{\mathrm{p}}$ is given by

$$\dot{\boldsymbol{\gamma}}^{\mathrm{p}} = \dot{\lambda}\frac{\partial f}{\partial \boldsymbol{\xi}} = 3\dot{\lambda}\boldsymbol{R}\boldsymbol{\xi} \tag{2.64}$$

At this point, it is convenient to define the isotropic Over Consolidation Ratio (OCR_p), which reflects the relationship between the initial preconsolidation pressure p_c and the current compressive pressure $-p$

$$\mathrm{OCR}_p = -\frac{p_c}{p} \tag{2.65}$$

Combination of definition in Eq. (2.65) with the plastic flow direction in Eq. (2.63) leads to the observation that when $\mathrm{OCR}_p < 2$ compaction is predicted while when $\mathrm{OCR}_p > 2$ dilatancy is predicted by Eq. (2.63).

Hardening/softening is determined from combination of Eqs. (2.60) and (2.58) and the condition that during loading a stress point remains on the yield surface. This results in the following form for the evolution of p_c

$$\frac{\dot{p}_c}{p_c} = \frac{-\dot{\varepsilon}_v^{\mathrm{p}}}{\lambda^* - \kappa^*} \tag{2.66}$$

Equation (2.66) shows that compaction leads to an increase of p_c (hardening) and dilatancy leads to a decrease of p_c (softening). This behavior is most conveniently illustrated with a conventional drained triaxial compression test. The stress path in the Rendulic plane, which is representative for this test, is shown in Figures 2.3 and 2.4. It is observed that when the initial value of the Over Consolidation Ratio is smaller than two ($p_{c,0}/p_0 < 2$) plastic compaction, and subsequently hardening behavior is observed (Figure 2.3). If, on the other hand, the initial Over Consolidation Ratio is significantly larger than two ($p_{c,0}/p_0 \gg 2$), plastic dilatancy and subsequently softening is predicted (Figure 2.4).

Figures 2.3 and 2.4 show that, for constant stress paths, eventually a state is reached where purely deviatoric flow is predicted. Subsequently, Eq. (2.66) predicts ideal plastic flow. Such a state is called the critical state and is identified by

$$\frac{q}{p} = -M \tag{2.67}$$

The Modified Cam-Clay model is most suitable for lightly overconsolidated clays, for which the compaction and hardening behavior are well predicted. A possible improvement which gives more accurate predictions for the coefficient of lateral earth pressure $K_0 =$
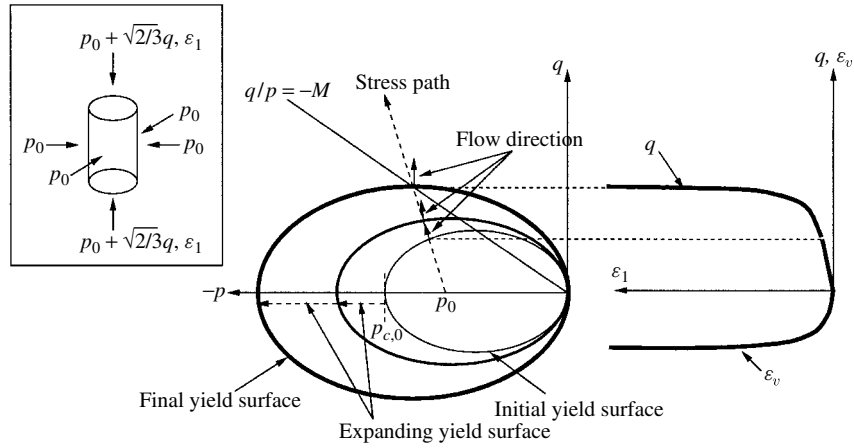
Figure 2.3   Drained triaxial compression $p_{c,0}/p_0 < 2$. The associative flow rule predicts compaction. Hence, Eq. (2.66) predicts hardening. Eventually, monotonic loading leads to a stress ratio $q/p = -M$, where purely deviatoric ideal plastic flow is predicted
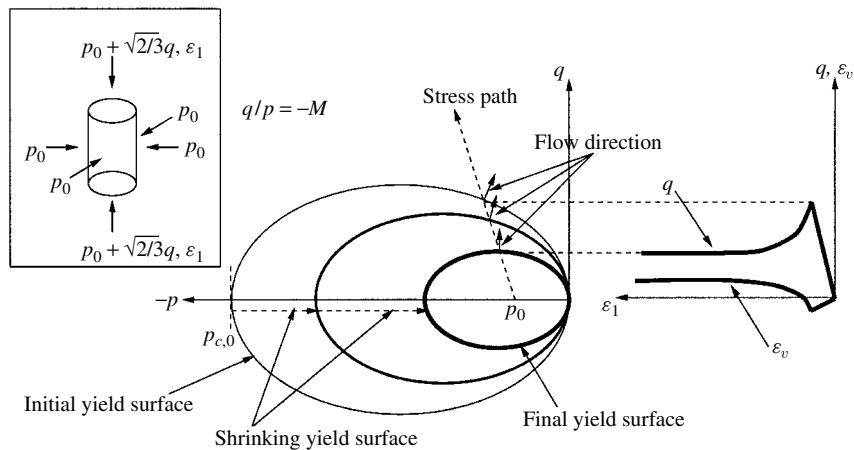
Figure 2.4   Drained triaxial compression $p_{c,0}/p_0 \gg 2$. The associative flow rule predicts dilatancy. Hence, Eq. (2.66) predicts softening. Eventually, monotonic loading leads to a stress ratio $q/p = -M$, where purely deviatoric ideal plastic flow is predicted

σ_h/σ_v can be found in Van Eekelen and Van den Berg (1994). For heavily overconsolidated clays, the prediction of the material behavior is less accurate (Wood, 1990).

2.4.1   Performance in laboratory tests

The deformation characteristics and the numerical performance are evaluated with four commonly known laboratory tests: Triaxial Compression (TC), Triaxial Extension (TE),

Pure Shear (PS) and Plane Strain Compression (PSC) (Figure 2.5). Instead of following the sign convention defined before, the sign convention for the stress components σ_1, σ_3 and for the strain component ε_1 is defined by Figure 2.5. All four tests have been simulated with a lightly overconsolidated material (initial isotropic Over Consolidation Ratio $OCR_{p,0} = 1.25$), and with a heavily over-consolidated material (initial isotropic Over Consolidation Ratio $OCR_{p,0} = 5$) with a cell pressure $\sigma_3 = 0.2$ MPa. The material parameters are adapted from Borja (1991) for Boston Blue Clay and are given by $\lambda^* = 0.032$, $\kappa^* = 0.013$, $M = 1.05$ and a Poisson's ratio $\nu = 0.2$.

The calculations have been performed with three different step sizes. The load-deformation and volume production-deformation curves are shown in Figure 2.6. As expected, all elementary tests predict hardening and compaction. The computed responses are nearly step size independent, which demonstrates the accuracy of the applied return-mapping algorithm. In Table 2.1, the average number of iterations required to reach an L_2-norm of 10^{-8} with respect to the initial L_2-norm of system of Eqs. (2.45)–(2.48) is displayed. Table 2.2 shows the convergence behavior in the equilibrium-finding iterative scheme for $OCR_{p,0} = 1.25$. It is observed that the convergence behavior is quadratic. Figure 2.7 shows the computed responses for $OCR_{p,0} = 5$. Except for the Plane Strain Compression test in Figure 2.7(d), which has a highly compressive stress path, all calculations show softening and dilatancy. As in the lightly overconsolidated case ($OCR_{p,0} = 1.25$) the computed responses are nearly step size independent. Table 2.3 shows the average number of iterations required to reach an L_2-norm of 10^{-8} with respect to the initial L_2-norm of system of Eqs. (2.45)–(2.48) for $OCR_{p,0} = 5$. Table 2.4 shows the convergence behavior in the equilibrium-finding iterative scheme for $OCR_{p,0} = 5$. Again, quadratic convergence is observed for the four laboratory tests.
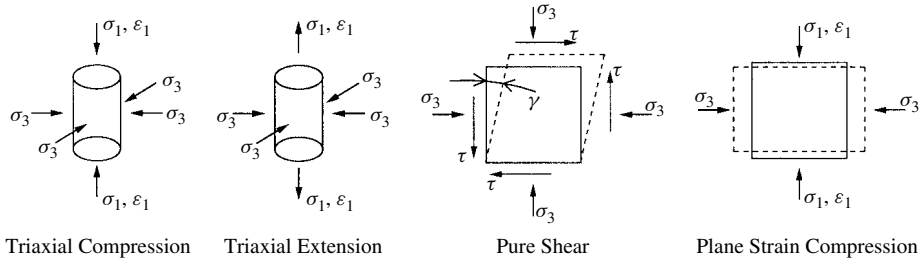
Figure 2.5 Four common laboratory tests. In the pure shear test and the plane strain compression test the out-of-plane strains are zero

Table 2.1 Average number of iterations required to reach an L_2-norm 10^{-8} with respect to the initial L_2-norm of the system (2.45)–(2.48) per equilibrium iteration, $OCR_{p,0} = 1.25$

|	CTC	TE	SS	PSC
10 steps	9	8.95	8.05	9
20 steps	7.91	7.87	7.02	7.93
200 steps	5.94	5.86	4.9	5.94
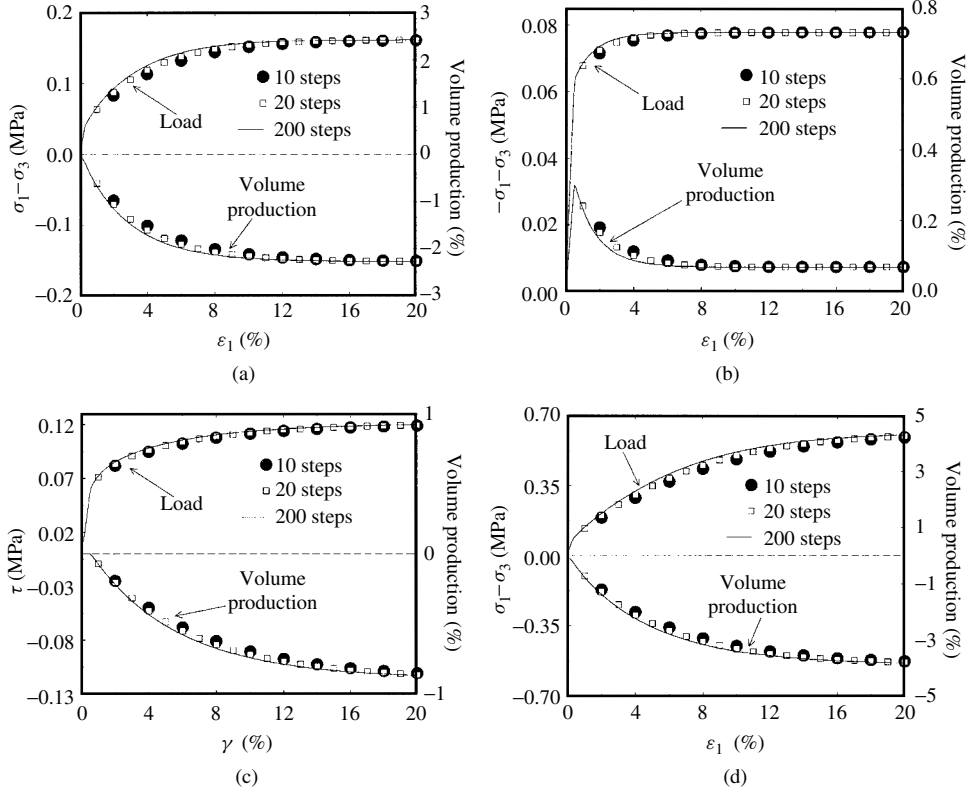
Figure 2.6 Simulation of laboratory tests with lightly overconsolidated material $OCR_{p,0} = 1.25$. (a) Triaxial compression (b) Triaxial Extension. (c) Pure Shear. (d) Plane Strain Compression

Table 2.2 Force norm in the equilibrium equations for 20 steps, $OCR_{p,0} = 1.25$

	CTC	TE	SS	PSC
Step 1	2.49×10^{-2} 6.16×10^{-5} 3.69×10^{-10}	2.93×10^{-1} 5.25×10^{-3} 1.77×10^{-6} 2.02×10^{-13}	1.36×10^{-1} 1.47×10^{-3} 2.42×10^{-7}	2.79×10^{-2} 1.24×10^{-4} 2.63×10^{-9}
Step 7	2.06×10^{-5} 2.13×10^{-10}	4.34×10^{-6} 3.05×10^{-12}	1.28×10^{-4} 2.48×10^{-9}	1.70×10^{-4} 3.73×10^{-8}
Step 20	7.50×10^{-9}	2.10×10^{-12}	1.00×10^{-6}	7.85×10^{-7}

2.4.2 Analysis of a guided pipe-jacking

In The Netherlands, the Drinking Water Service Company of the province of South Holland has constructed a pipeline system of approximately 60 km using a guided pipe-jacking method. The resulting surface settlements have been measured (van der Broek
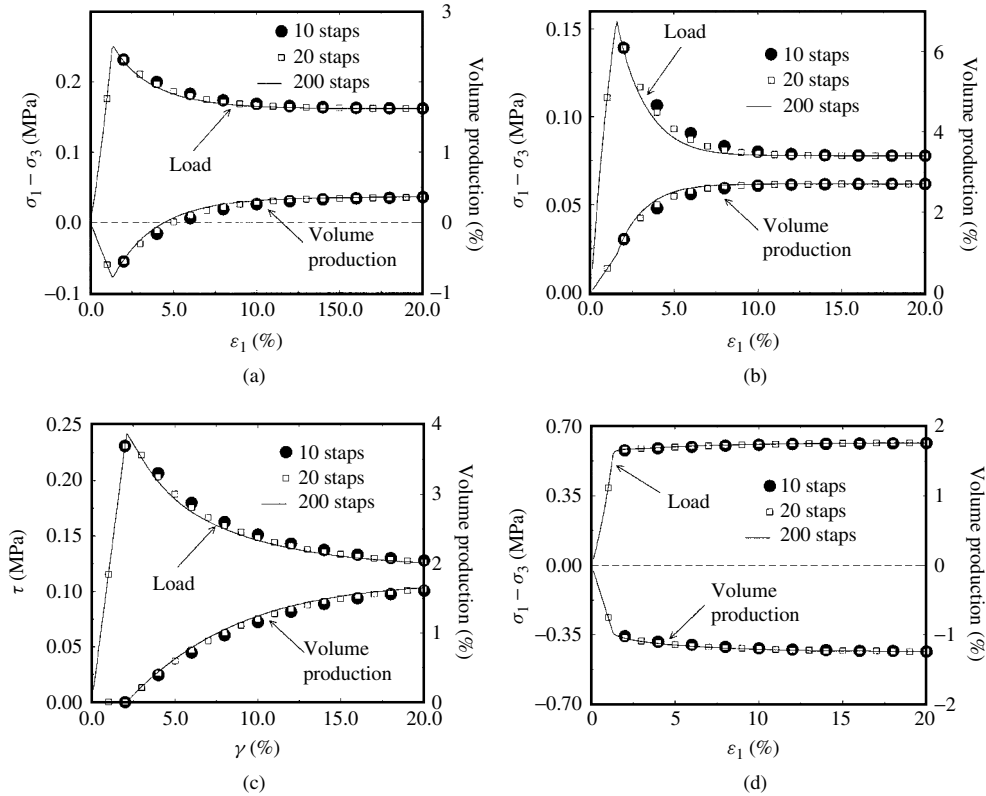
Figure 2.7 Simulation of laboratory tests with heavily overconsolidated material $OCR_{p,0} = 5$. (a) Triaxial compression. (b) Triaxial Extension. (c) Pure Shear. (d) Plane Strain Compression

Table 2.3 Average number of iterations required to reach an L_2-norm 10^{-8} with respect to the initial L_2-norm of system (2.45)–(2.48) per equilibrium iteration, $OCR_{p,0} = 5$

	CTC	TE	SS	PSC
10 steps	8.43	8.56	7.43	8.44
20 steps	7.62	7.35	6.63	7.57
200 steps	5.58	5.2	4.56	5.63

et al., 1996). A three-dimensional analysis is utilized for the prediction of the surface settlements.

Two top deposits have been modeled. The tunnel has a diameter of two meters, and is located in the lower deposit with its center at seven meters below the surface. The interface between the upper deposit and the lower deposit is located two meters below the surface.

Table 2.4   Force norm in the equilibrium equations for 20 steps, $\text{OCR}_{p,0} = 5$

	CTC	TE	SS	PSC
Step 3	1.30×10^{-2}	8.03×10^{-2}	1.37×10^{-1}	2.50×10^{-3}
	1.42×10^{-4}	2.96×10^{-3}	1.13×10^{-2}	1.15×10^{-5}
	1.64×10^{-8}	3.64×10^{-6}	9.98×10^{-5}	2.50×10^{-10}
		5.54×10^{-12}	7.97×10^{-9}	
Step 10	2.46×10^{-6}	1.44×10^{-5}	9.95×10^{-5}	1.45×10^{-7}
	3.72×10^{-12}	3.42×10^{-11}	3.91×10^{-9}	
Step 20	3.75×10^{-9}	6.78×10^{-10}	8.38×10^{-6}	3.80×10^{-9}
			1.93×10^{-11}	

For the upper deposit, a compression index $\lambda^* = 0.15$ and a swelling index $\kappa^* = 0.015$ have been assumed. For the lower deposit $\lambda^* = 0.15$ and $\kappa^* = 0.03$ are adopted. Furthermore, $M = 0.877$, a density of $15 \, \text{kN/m}^3$, an initial isotropic Over Consolidation Ratio $\text{OCR}_{p,0} = 1.1$ and a Poisson's ratio $\nu = 0.2$ are adopted for both deposits. $\overline{\boldsymbol{B}}$-elements (Hughes, 1980) have been applied.

Two types of analysis have been performed: (a) a drained analysis, in which it is assumed that the soil skeleton is completely responsible for the deformation behavior of the structure; (b) an undrained analysis, in which it is assumed that the deformations are determined by parallel action of soil and water content. Under undrained conditions the water content enforces a zero volume change upon the deformations, both in the elastic and in the plastic regime.

The calculation has been performed in three phases:

(1) **Drained, one step** The gravity load is applied. It has been assumed that the tunnel lining is already present but has no weight yet. The tunnel lining has been assumed as rigid. The weight of the soil is modeled by a point-load downwards. Moreover, it is assumed that the Tunnel Boring Machine is in-line with the tunnel lining. After the gravity load is applied, the horizontal stresses are calculated with a coefficient of lateral earth pressure $K_0 = \sigma_h / \sigma_v = 0.6$.

(2) **Drained/undrained, four steps** The weight of the tunnel lining is applied simultaneously with the removal of the weight of the soil in the tunnel in four steps. This has been simulated by application of a net load [WEIGHT TUNNEL LINING – WEIGHT SOIL] downwards. As the tunnel lining is lighter than the removed soil this results in an uplift of the tunnel lining and Tunnel Boring Machine (Figure 2.8(a)).

(3) **Drained/undrained, twenty-five steps** Pregrouting loss around the tunnel lining is simulated by contraction of the tunnel lining which has been assumed to be ten percent of the volume of the tunnel. Loss due to the boring process is simulated by a contraction of seven percent of the volume of the tunnel around the Tunnel Boring Machine (TBM) (Figure 2.8(b)). The tunnel boring front has been supported by an overburden pressure of 0.1 bar, typical for the guided pipe-jacking method.
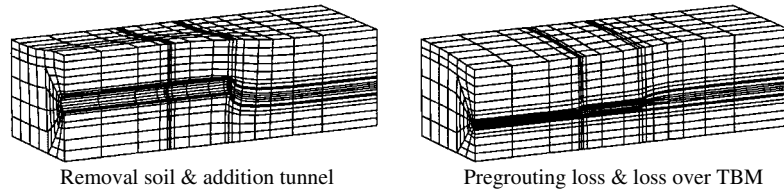
Removal soil & addition tunnel   Pregrouting loss & loss over TBM

Figure 2.8   Deformations at the different phases of the loading process

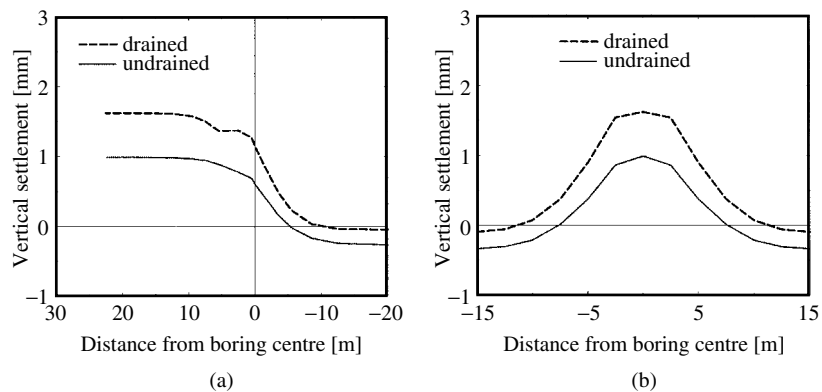(a)   (b)

Figure 2.9   Surface settlements after the removal of soil and addition of the tunnel lining for the undrained analysis. (a) Settlements parallel to the tunnel. (b) Settlements 22.5 m behind the front of the Tunnel Boring Machine

Not all factors that influence the deformation have been taken into account; for instance, consolidation effects, the stiffness of tunnel lining and Tunnel Boring Machine and steering effects of the Tunnel Boring Machine have not been considered. However, the primary objectives of this simulation are: (a) to give at least a qualitative representation of the surface settlements; and (b) to assess the performance of the return-mapping algorithm presented before.

Figure 2.9 shows the surface settlements after phase two (removal of the soil and addition of the tunnel lining), and Figure 2.10 shows the surface settlements after phase 3 (contraction of the tunnel lining and Tunnel Boring Machine). It is observed from Figure 2.9 that the surface settlements under drained conditions are larger than under undrained conditions. This can be attributed to the fact that under undrained conditions the water content acts parallel to the soil skeleton which results in a stiffer behavior. From Figure 2.10, it is observed that the surface settlements under drained conditions are also larger than under undrained conditions. Since the loading in this phase is deformation controlled, this cannot be attributed to an increased stiffness due to the water content. Here, the smaller surface settlement under undrained conditions can be attributed to the fact that the water content enforces volume preserving deformations upon the soil skeleton. Since very lightly over-consolidated material has been adopted, drained conditions result in compaction and thus in larger surface settlements.
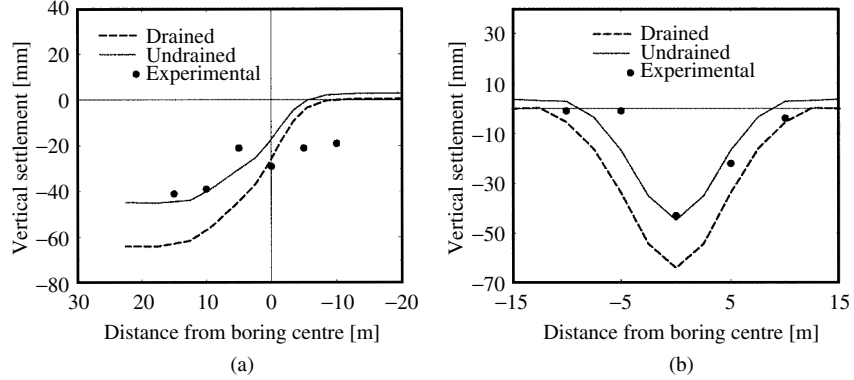
Figure 2.10   Surface settlements resulting from pregrouting loss and loss over the Tunnel Boring Machine. (a) Settlements parallel to the tunnel. (b) Settlements 22.5 m behind the front of the Tunnel Boring Machine

2.5   Modeling of Sand

While the Modified Cam-Clay model is able to capture a large number of phenomena that occur in clayey soils with only a few parameters, it cannot describe typical phenomena that occur in sands such as simultaneous hardening and dilatancy. A possible extension would be to assume that the plastic behavior in shear is independent from the behavior in compression. This approach was first suggested by Drucker *et al.* (1957), who suggested a spherical cap on the Drucker–Prager yield surface. Later, Dimaggio and Sandler (1971), Lade (1977), Molenkamp (1980) and Vermeer (1980) followed the same approach in which, in addition to shear failure, compressive deformations were modeled by a cap. More recent models integrate the shear and compressive behavior into a single surface (Desai, 1980, Kim and Lade, 1988, Lade and Kim, 1988a,b).

Here, the plastic behavior in shear and in compression will be modeled independently. This allows the formulation of a model which remains close to established concepts such as Rowe's stress-dilatancy theory (Rowe, 1962), and the formulation of the compressive behavior similar to the Modified Cam-Clay model.
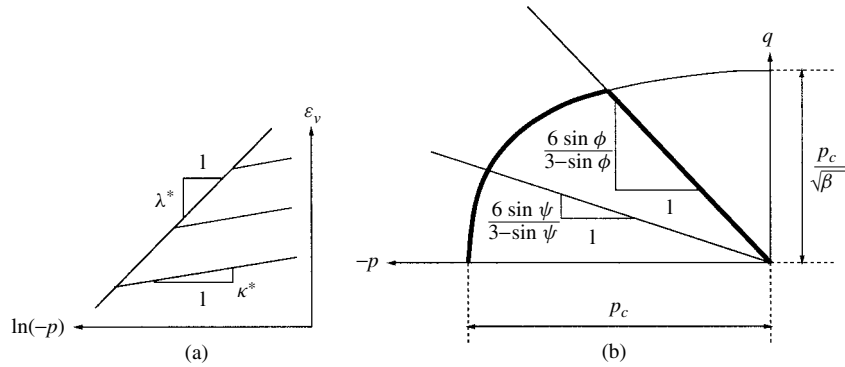
Analogous to the Modified Cam-Clay model, an increasing bulk stiffness for increasing compression is modeled by

$$\dot{p} = -\frac{p}{\lambda^*}\dot{\varepsilon}_v = K_t\dot{\varepsilon}_v \text{ loading} \tag{2.68}$$

$$\dot{p} = -\frac{p}{\kappa^*}\dot{\varepsilon}_v = K_t\dot{\varepsilon}_v \text{ unloading} \tag{2.69}$$

with λ^* the 'modified compression index' and κ^* the 'modified swelling index' (Figure 2.11(a)). As elastic unloading is assumed Eq. (2.69) can be expressed in elastic components only

$$\dot{p} = -\frac{p}{\kappa^*}\dot{\varepsilon}_v^e = K_t\dot{\varepsilon}_v^e \tag{2.70}$$

Figure 2.11   Material description for the double-hardening model. (a) Compressive behavior. (b) Yield function and plastic potential

Equation (2.70), together with the assumption of isotropy and a constant Poisson's ratio ν, gives the following expression for the tangent shear modulus G_t

$$G_t = \frac{3}{2}\frac{1-2\nu}{1+\nu}K_t \tag{2.71}$$

Shear failure is assumed to occur on a Drucker–Prager type failure surface

$$f_1 = \left(\frac{1-\alpha\cos 3\theta}{1-\alpha}\right)^{-n} q + \frac{6\sin\phi}{3-\sin\phi}p \tag{2.72}$$

in which ϕ is the friction angle, and α and n are parameters which include the effect of the Lode angle θ. A projection of the yield function in Eq. (2.72) on the deviatoric plane is shown in Figure 2.12. Optimal properties regarding convexity are obtained when $n = -0.229$ (van Eekelen, 1980). Convexity is then retained for $\alpha \leq 0.7925$, which corresponds to a fit through all the corners of the Mohr–Coulomb criterion for a friction angle of $46.55°$.
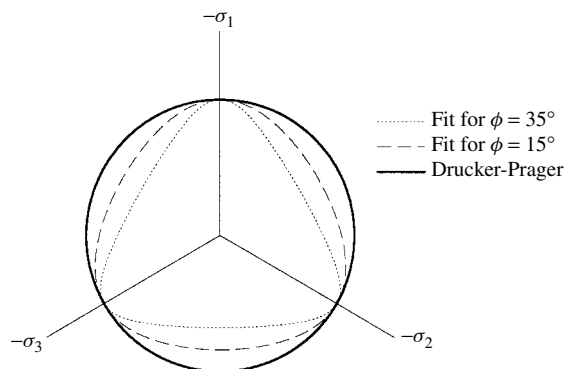
Figure 2.12   Yield function (2.72) in the deviatoric plane

Plastic flow on the shear failure surface given by Eq. (2.72) is assumed to be non-associative, and is determined by the Drucker–Prager plastic potential

$$g_1 = q + \frac{6 \sin \psi}{3 - \sin \psi} p \qquad (2.73)$$

in which ψ is the dilatancy angle. This assumption of a Drucker–Prager plastic potential is motivated by experimental results from Kim and Lade (1988) which indicate a plastic potential close to a Drucker–Prager contour in the deviatoric plane.

During compaction, plastic straining is described by the compression cap

$$f_2 = p^2 + \beta q^2 - p_c^2 \qquad (2.74)$$

where associative plasticity is assumed. In Eq. (2.74), β is a shape parameter (van Langen, 1991) which is used to fit the prediction of the coefficient of lateral earth pressure $K_0 = \sigma_h/\sigma_v$. p_c is a measure for the current degree of over-consolidation and can be determined from an isotropic Over Consolidation Ratio (OCR$_p$) similar to the Modified Cam-Clay model

$$\text{OCR}_p = -\frac{p_c}{p} \qquad (2.75)$$

or alternatively, from an Over Consolidation Ratio (OCR) which is based on the size of the cap in Eq. (2.74), and thus includes the effect of the effective deviatoric stress:

$$\text{OCR} = -\frac{p_c}{\sqrt{p^2 + \beta q^2}} \qquad (2.76)$$

The yield functions given by Eqs. (2.72) and (2.74) and the plastic potential in Eq. (2.73) have been plotted in Figure 2.11(b).

The plastic strain rates are assumed to be an additive decomposition of plastic strain rates $\boldsymbol{\varepsilon}_1^p$ on the shear failure surface given by Eq. (2.72) and plastic rates $\boldsymbol{\varepsilon}_2^p$ on the compression cap in Eq. (2.74).

$$\dot{\boldsymbol{\varepsilon}}^p = \dot{\boldsymbol{\varepsilon}}_1^p + \dot{\boldsymbol{\varepsilon}}_2^p \qquad (2.77)$$

This leads to the following expression for the volumetric plastic strain rates

$$\dot{\varepsilon}_v^p = \dot{\lambda}_1 \frac{\partial g_1}{\partial p} + \dot{\lambda}_2 \frac{\partial f_2}{\partial p} = \dot{\lambda}_1 \frac{6 \sin \psi}{3 - \sin \psi} + 2 p \dot{\lambda}_2 \qquad (2.78)$$

and for the deviatoric plastic strain rates

$$\dot{\boldsymbol{\gamma}}^p = \dot{\lambda}_1 \frac{\partial g_1}{\partial \boldsymbol{\xi}} + \dot{\lambda}_2 \frac{\partial f_2}{\partial \boldsymbol{\xi}} = \dot{\lambda}_1 \frac{3}{2} \frac{\boldsymbol{R}\boldsymbol{\xi}}{q} + \dot{\lambda}_2 3 \boldsymbol{R}\boldsymbol{\xi} \qquad (2.79)$$

Friction hardening is assumed according to

$$\sin \phi = \sin \phi(\gamma_{eff}^p) \qquad (2.80)$$

in which γ_{eff}^p is defined as the effective deviatoric plastic strain on the failure surface (Vermeer, 1980), and is defined in a rate form as

$$\dot{\gamma}_{eff}^p = \sqrt{\tfrac{2}{3} \dot{\boldsymbol{\gamma}}_1^{pT} \boldsymbol{R}^{-1} \dot{\boldsymbol{\gamma}}_1^p} \qquad (2.81)$$

Equation (2.81) leads to a convenient relationship between the rate of the plastic multiplier on the failure surface $\dot{\lambda}_1$ and $\dot{\gamma}^p_{eff}$

$$\dot{\gamma}^p_{eff} = \dot{\lambda}_1 \tag{2.82}$$

Dilatancy is assumed to obey Rowe's stress-dilatancy theory in triaxial compression

$$\sin \psi = \frac{\sin \phi - \sin \phi_{cv}}{1 - \sin \phi \sin \phi_{cv}} \tag{2.83}$$

in which ϕ_{cv} is identified as the so-called 'friction angle at constant volume' (Vermeer and de Borst, 1984). The evolution of hardening on the cap defined by Eq. (2.74) is derived from the loading function in Eqs. (2.68) and (2.70) and the condition that during compressive loading a stress point is located on the cap in Eq. (2.74). This results in the following form for the evolution of p_c:

$$\frac{\dot{p}_c}{p_c} = \frac{-\dot{\varepsilon}^p_{v,2}}{\lambda^* - \kappa^*} \tag{2.84}$$

in which $\dot{\varepsilon}^p_{v,2}$ is the plastic volumetric strain rate on the cap.

2.5.1 Performance in laboratory tests

The numerical performance of the proposed integration algorithm has been evaluated for four elementary tests, namely Conventional Triaxial Compression (CTC), Triaxial Extension (TE), Simple Shear (SS) and Plane Strain Compression (PSC) (Figure 2.13).

The adopted material parameters are $\kappa^* = 0.00573$, $\lambda^* = 0.00693$, $\nu = 0.18$, $\beta = 2/9$ and $\phi_{cv} = 30.66°$. Furthermore, the specimens are isotropically consolidated with a cell pressure $\sigma_3 = 0.2$ MPa and the shape factor $\alpha = 0.689$, which corresponds to a smooth fit through all the corners of the Mohr–Coulomb yield surface for a friction angle $\phi = 35°$. A multi-linear friction hardening diagram is used (Table 2.5).

The calculations have been performed with three different step sizes. The load-deformation curves are shown in Figure 2.14. It is observed that the solution is practically independent of the step size.
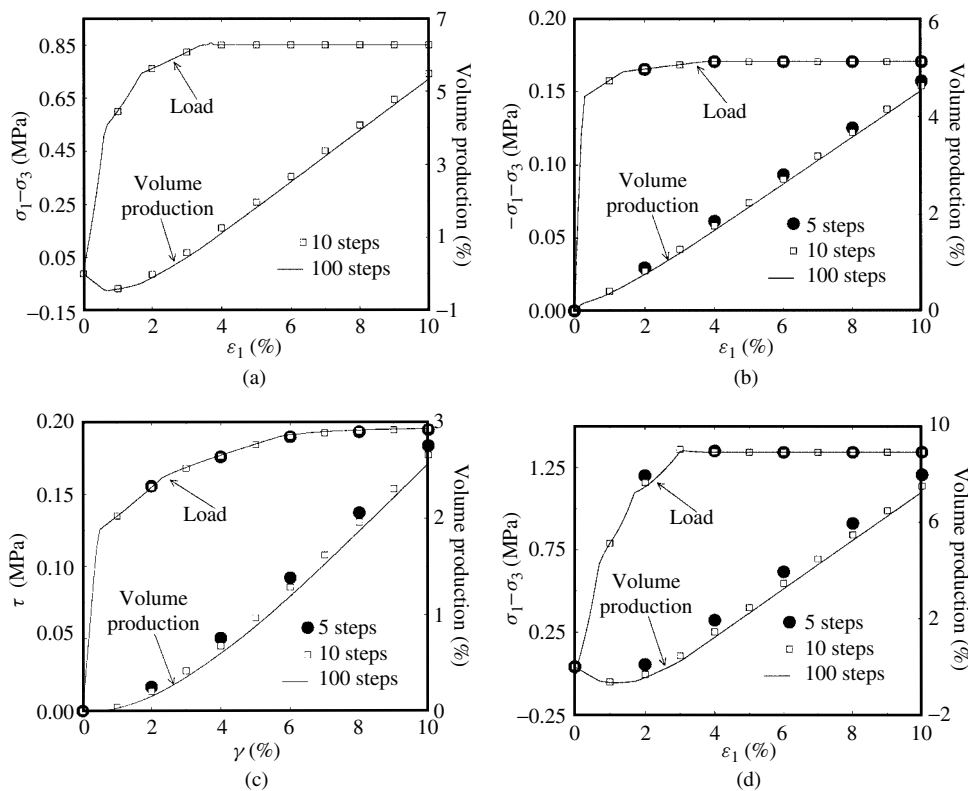
Table 2.6 shows the average number of iterations required to reach an L_2-norm of 10^{-8} with respect to the initial L_2-norm of system of Eqs. (2.45)–(2.48). Table 2.7 shows the
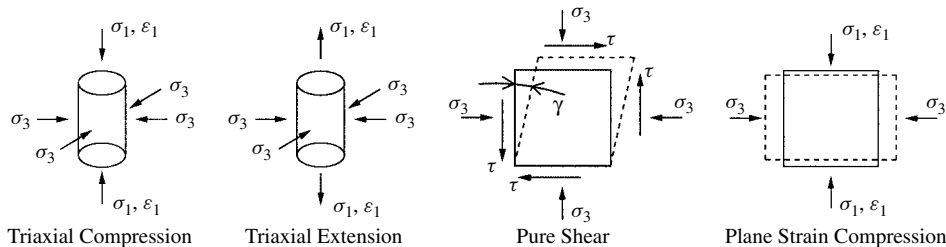
Figure 2.13 Four common laboratory tests. In the pure shear test and the plane strain compression test the out-of-plane strains are zero

Table 2.5   Multi-linear friction hardening diagram

ϕ (degrees)	35.03	40.54	42.84	42.84
γ_{eff}^{p}	0.0	0.01	0.03	∞

Figure 2.14   Simulation of laboratory tests. (a) Triaxial Compression. (b) Triaxial Extension. (c) Pure Shear. (d) Plane Strain Compression

Table 2.6   Average number of iterations required to reach an L_2-norm 10^{-8} with respect to the initial L_2-norm of the system (2.45)–(2.48) per equilibrium iteration

	CTC	TE	SS	PSC
5 steps	X	8.36	8.38	10.14
10 steps	7.8	5.75	8.88	8.5
100 steps	4.31	3.93	3.97	4

Table 2.7 Force norm in the equilibrium equations for ten steps

	CTC	TE	SS	PSC
Step 1	1.30×10^{-1}	5.61×10^{-1}	8.87×10^{-2}	4.94×10^{-2}
	1.67×10^{-2}	1.81×10^{-1}	3.52×10^{-3}	8.43×10^{-3}
	3.84×10^{-4}	8.80×10^{-3}	6.27×10^{-6}	3.25×10^{-4}
	2.16×10^{-7}	2.37×10^{-5}	1.07×10^{-11}	5.17×10^{-7}
		1.75×10^{-10}		
Step 3	3.82×10^{-3}	1.54×10^{-3}	3.19×10^{-2}	4.06×10^{-3}
	1.99×10^{-5}	6.07×10^{-7}	7.29×10^{-4}	7.32×10^{-5}
	5.49×10^{-10}		3.59×10^{-7}	1.13×10^{-7}
Step 10	3.60×10^{-7}	3.59×10^{-10}	8.31×10^{-6}	6.12×10^{-8}
			7.51×10^{-11}	

convergence in the force norm of the equilibrium equations. Except for the CTC test with the largest step size, for which no convergence could be obtained, excellent convergence behavior is observed both in the solution of the system of Eqs. (2.45)–(2.48) as well as in the solution of the equilibrium equations.

2.5.2 Analysis of the Leaning Tower of Pisa

The Leaning Tower of Pisa is one of the most challenging problems in geomechanics. The geotechnical profile and the essentially three-dimensional deformation behavior makes it an excellent test case to verify the applicability of the double-hardening model and the robustness and performance of the applied integration algorithm. A three-dimensional numerical simulation has been carried out in order to investigate the effect of the lead blocks that have been applied on the high-side of the tower in 1993 to reduce the inclination.

It is not the objective to give a quantitative representation of the deformations under the tower. The geotechnical conditions as well as the loading conditions on the foundation of the tower are simply too complicated. Moreover, the uncertainty in the constitutive parameters is too large to give any realistic prediction of the true deformations that occur in the subsoil under the tower. However, the three-dimensional character as well as the relatively clear classification of the constitutive parameters makes the Leaning Tower of Pisa an excellent benchmark for assessment of the performance of the adopted double-hardening model.

Calabresi *et al.* (1993) have performed triaxial tests on the soil deposits underneath the tower and have proposed Modified Cam-Clay parameters for the clayey deposits and Mohr–Coulomb frictional parameters for the sandy deposits. The material parameters proposed by Calabresi *et al.* (1993) are adapted to the double-hardening model (Table 2.8).

It is assumed that the respective friction angles do not change during the loading process. The parameter α is adjusted such that a fit through all the corners of the Mohr–Coulomb yield function is obtained for each deposit. Furthermore, a dilatancy angle $\psi = 0$ and a Poisson's ratio $\nu = 0.12$ are assumed for all deposits.

The foundation of the tower is assumed to have a density $\rho = 21.43$ kN/m^3, a Young's modulus of $E = 1.5 \times 10^6$ kPa, a Poisson's ratio $\nu = 0.12$ and a coefficient of lateral earth pressure $K_0 = 0.9231$.

Table 2.8 Material properties for the respective deposits under the tower. The material parameters proposed by Calabresi *et al*. (1993) are adapted to the double-hardening model

Depth [m]	E[kPa]	κ^*	λ^*	$\sin(\phi)$	OCR	K_0	ρ[kN/m^3]
0–1.4	–	0.00486	0.0481	0.555	4.2	0.9231	21.43
1.4–5.4	–	0.00495	0.049	0.554	3.0	0.7857	19.17
5.4–7.4	1.25×10^4	–	–	0.559	–	0.4493	15.40
7.4–17.8	–	0.014	0.107	0.446	1.35	0.6949	18.49
17.8–22	–	0.0151	0.0722	0.479	1.8	0.6667	19.64
22–24.4	1.8×10^4	–	–	0.564	–	0.4286	20.40
24.4–37	–	0.0106	0.0851	0.424	1.1	0.5625	21.66

Table 2.9 Material properties for the respective deposits under the tower. The compressive indices in Calabresi *et al*. (1993) are approximated by a linear elastic compressive stiffness based on the initial stress state (Grashuis, 1993)

Depth [m]	E[kPa]	$\sin(\phi)$	K_0	ρ[kN/m^3]
0–1.4	3×10^3	0.555	0.9231	21.43
1.4–5.4	3×10^3	0.554	0.7857	19.17
5.4–7.4	1.25×10^4	0.559	0.4493	15.40
7.4–17.8	8×10^3	0.446	0.6949	18.49
17.8–22	1.4×10^4	0.479	0.6667	19.64
22–24.4	1.8×10^4	0.564	0.4286	20.40
24.4–37	2.5×10^4	0.424	0.5625	21.66

Alternatively, a set of material properties has been used with a linear elastic approximation for the compressive behavior (Grashuis, 1993) (Table 2.9).

As for the guided pipe-jacking, the analysis has been performed with $\overline{\boldsymbol{B}}$-elements (Hughes, 1980).

The vertical stress state under the tower is initialized with the self-weight of the soil skeleton. The horizontal stresses are then calculated with the coefficient of lateral earth pressure $K_0 = \sigma_h/\sigma_v$. Drained conditions have been assumed (i.e. no influence of the ground water on the deformation behavior). Hereafter, the loading history is simulated by three phases:

1. The weight of the tower is applied in twenty-nine steps under drained conditions.
2. The moment on the foundation due to the inclination of the tower is applied in twenty steps under drained conditions.
3. The weight and the moment due to the lead-blocks are applied in eight steps. Both drained conditions and undrained conditions are simulated.

Figure 2.15 shows the incremental deformations after each loading phase for the material properties in Table 2.8. Figure 2.16 shows the applied moment versus the inclination of the tower. From Figure 2.16 it is observed that the material parameters listed in Table 2.8 give an inclination of approximately 1.2°, while the simulation with the material

(a)   (b)

(c)   (d)
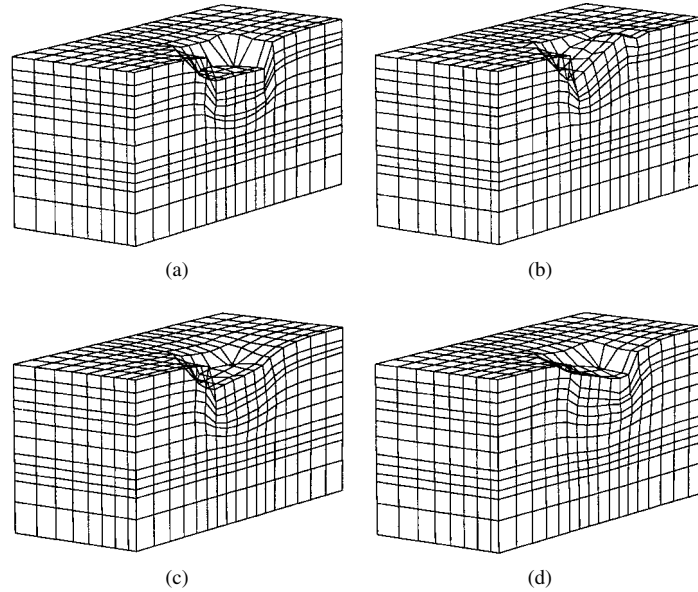
Figure 2.15 Incremental deformations for the material properties listed in Table 2.8 (double-hardening model for the clayey layers). (a) After application of the weight of the tower. (b) After application of the moment due to the inclination of the tower. (c) After application of the lead-blocks on the high side of the tower under drained conditions. (d) After application of the lead-blocks on the high side of the tower under undrained conditions

(a)   (b)
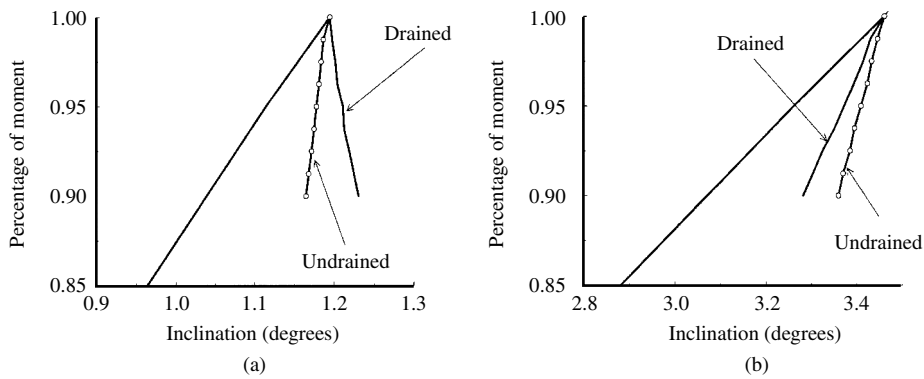
Figure 2.16 Moment versus inclination of the tower. (a) Utilizing the material parameters from Table 2.8. (b) Utilizing the material parameters from Table 2.9

parameters listed in Table 2.9 gives a much softer response (an inclination of approximately 3.5°). A salient feature which can be observed both from Figure 2.15(c), as well as from Figure 2.16(a) is that the material properties listed in Table 2.8 result in an increase of the inclination of the tower under drained conditions during application of the lead blocks.

2.6   Conclusions

A fully implicit Euler backward integration rule has been developed with the use of stress invariants and elastic secant moduli. The algorithm is conveniently implemented within a finite element framework and is applicable to a wide range of models that are representative for soils. Elementary tests under different monotonic loading conditions demonstrate the numerical performance and accuracy of the proposed integration algorithm. The robustness has been assessed by the analysis of realistic boundary value problems which indicate that indeed solutions can be obtained for relatively large loading steps.

Acknowledgements

References

Borja, R. Cam-clay plasticity, Part II, Implicit integration of constitutive equations based on a nonlinear elastic stress predictor. *Comp. Meth. Appl. Mech. Engng.*, **88**, (1991) 225–240.

Britto, A.M and Gunn, M.J. *Critical State Soil Mechanics via Finite Elements*. Ellis Horwood, Chichester, (1987).

Calabresi, G., Rampello, S. and Callisto, L. The leaning tower of Pisa, geotechnical characterisation of the tower's subsoil within the framework of the critical state theory. *Studi e Recherche, Universita degli Roma 'La Sapienza'*, (1993).

de Borst, R and Feenstra, P.H. Studies in anisotropic plasticity with reference to the Hill criterion. *Int. J. Num. Meth. Engng.*, **29**, (1990) 315–336.

Desai, C.S. A general basis for yield, failure and potential functions in plasticity. *Int. J. Num. Anal. Meth. Geom.*, **4**, (1980) 361–375.

Desai, C.S., Sharma, K.G., Wathugala, G.W. and Rigby, D.B. Implementation of hierarchical single surface δ_0 and δ_1 models in finite element procedure. *Int. J. Num. Anal. Meth. Geom.*, **15**, (1991) 649–680.

DiMaggio, F.L and Sandler, I.V. Material model for granular soils. *J. Engng. Mech. Div. ASCE*, **97**, (1971) 935–950.

Drucker, D.C, Gibson, R.E. and Henkel, D.J. Soil mechanics and work hardening theories of plasticity. *Trans. ASCE*, **122**, (1957) 338–346.

Feenstra, P.H. *Computational aspects of biaxial stress in plane and reinforced concrete*. Dissertation, Delft University of Technology, (1993).

Grashuis, A.J. Pisa–Toren berekening en validatie Pluto-3D. *Report SE-57013*, Delft Geotechnics, (1993).

Hicks, M.A. MONICA-A computer algorithm for solving boundary value problems using the double hardening constitutive law MONOT: I. Algorithm development. *Int. J. Num. Anal. Meth. Geom.*, **19**, (1995) 1–27.

Hofstetter, G., Simo, J.C. and Taylor, R.L. A modified cap model: Closest point solution algorithms. *Comp. Struct.*, **46**(2), (1993) 203–214.

Hughes, T.J.R. Generalization of selective integration procedures to anisotropic and nonlinear media, *Int. J. Num. Meth. Eng.*, **15**, (1980) 1413–1418.

Kim, M.K. and Lade, P.V. Single hardening constitutive model for frictional materials I. Plastic potential function. *Computers and Geotechnics*, **5**, (1988) 307–324.

Koiter, W.T. Stress-strain relations, uniqueness and variational problems for elastic-plastic materials with singular yield surface. *Q. Appl. Math.*, **11**, (1953) 350–354.

Lade, P.V. Elasto-plastic stress-strain theory for cohesionless soil with curved yield surfaces. *Int. J. Sol. Struct.*, **13**, (1977) 1019–1035.

Lade, P.V. and Kim, M.K. Single hardening constitutive model for frictional materials II. Yield criterion and plastic work contours. *Computers and Geotechnics*, **6**, (1988a) 13–29.

Lade, P.V. and Kim, M.K. Single hardening constitutive model for frictional materials III. Comparisons with experimental data. *Computers and Geotechnics*, **6**, (1988b) 31–47.

Lourenço, P.B. *Computational strategies for masonry structures*. Dissertation, Delft University of Technology, (1996).

Matsuoka, H. and Nakai, T. Stress-deformation and strength characteristics of soil under three different principal stresses. *Proc. JSCE*, **232**, (1974) 59–70.

Molenkamp, F. Elasto-plastic double hardening model MONOT. *LGM Report CO-218595*, Delft Geotechnics, (1980).

Ortiz, M. and Popov, E.P. Accuracy and stability of integration algorithms for elastoplastic constitutive relations. *Int. J. Num. Meth. Engng.*, **28**, (1985) 461–474.

Roscoe, K.H. and Burland, J.B. On the generalized behaviour of 'wet' clay. *Engineering Plasticity*, **48**, (1968) 535–609.

Roscoe, K.H. and Schofield, A.N. Mechanical behaviour of an idealised 'wet' clay. *Proc. European Conf. on Soil Mechanics and Foundation Engineering*, Wiesbaden, **1**, (1963) 47–54.

Rowe, P.W. The stress-dilatancy relation for static equilibrium of an assembly of particles in contact. *Proc. Roy. Soc. London*, **A269**, (1962) 500–527.

Schellekens, J.C.J. and de Borst, R. The use of the Hoffmann yield criterion in finite element analysis of anisotropic composites. *Comp. Struct.*, **37**(6), (1990) 1087–1096.

Schofield, A.N. and Wroth, C.P. *Critical State Soil Mechanics.* McGraw Hill, London, (1968).

Simo, J.C. and Meschke, G. A new class of algorithms for classical plasticity extended to finite strains. Application to geomaterials. *Computational Mechanics*, **11**, (1993) 253–278.

Simo, J.C. and Taylor, R.L. A return mapping algorithm for plane stress elastoplasticity. *Int. J. Num. Meth. Engng.*, **22**, (1986) 649–670.

Simo, J.C. Kennedy, J.G. and Govindjee, S. Non-smooth multisurface plasticity and viscoplasticity. Loading/unloading conditions and numerical algorithms. *Int. J. Num. Meth. Engng.*, **26**, (1988) 2161–2185.

van den Broek, W.L.A.H., de Borst, R. and Groen, A.E. Two- and three-dimensional modelling of a guided pipe-jacking in soft soil. *Geotechnical Aspects of Underground Construction in Soft Ground*. Balkema, Rotterdam, (1996) 419–422.

van Eekelen, H.A.M. Isotropic yield surfaces in three dimensions for use in soil mechanics. *Int. J. Num. Anal. Meth. Geom.*, **4**, (1980) 89–101.

van Eekelen, S.J.M. and van den Berg, P. The Delft egg model, a constitutive model for clay. In: *DIANA Computational Mechanics '94*, Kusters, G.M.A. and Hendriks, M.A.N. (eds.), Kluwer Academic Dordrecht, (1994) 103–116.

van Langen, H. *Numerical analysis of soil-structure interaction*. Dissertation, Delft University of Technology, (1991).

Vermeer, P.A. *Formulation and analysis of sand deformation problems*. Dissertation, Delft University of Technology, (1980).

Vermeer, P.A. and de Borst, P. Non-associated plasticity for soils, concrete and rock. *Heron*, **29**(3), (1984) 1–64.

Wood, D.M. *Soil Behaviour and Critical State Soil Mechanics*. Cambridge University Press, Cambridge, (1990).

Zytinsky, M., Randolph, M.K., Nova, R. and Wroth, C.P. On modelling the unloading-reloading behaviour of soils. *Int. J. Num. Anal. Meth. Geom.*, **2**, (1978) 87–93.